npj | materials degradation

Article

Published in partnership with CSCP and USTB

https://doi.org/10.1038/s41529-026-00827-3

The ambient- and high-temperature oxidation behaviour of $U^{3+}N$ and $Ln^{3+}N$ compounds relevant to spent nuclear fuel

Pascal Uhlemann[1] ✉, Emily M. Reynolds[2], Martina Klinkenberg[1], Damien Prieur[3,4], Christian Schreinemachers[1], Philip Kegler[1], Celina Erven[1], Sven M. Schenk[2], Joerg Göttlicher[5], Ralph Steininger[5], Mary Blankenship[5,6], Lothar Weinhardt[5,6,7], Nina Huittinen[3,8], Peter Höhn[9], Tonya Vitova[2], Giuseppe Modolo[1] & Gabriel L. Murphy[1] ✉

Actinide and lanthanide binary nitrides (*An*N, *Ln*N), are isostructural cubic compounds relevant to next-generation nuclear fuels which require detailed understanding regarding their oxidative degradation for safe disposal, yet a systematic comparative description remains. Herein, the room- and high-temperature oxidation behaviour of $U^{3+}N$ and $Ln^{3+}N$ (*Ln* = Pr, Nd, Gd, Tb, Dy, Ho, Tm and Lu) compounds is examined via a combination of X-ray diffraction, electron microscopy, thermogravimetric, and X-ray absorption spectroscopy analysis. At room temperature, UN was found to undergo an oxygen mediated oxidising mechanism, which contrasted chemically and microstructurally to the *Ln*N's, which followed a consistent hydrolysis mechanism. At high temperature, more congruent behaviour is determined with direct occurrence of oxide products, where the onset temperature of oxidation was found to correlate with the ionic radii of examined *Ln*/U cations. The results provide insight into the behaviour of these compounds in UN-based spent fuel, particularly phase separation variability and incongruent behaviour during inadvertent oxidation.

Uranium nitride, UN, has attracted considerable attention regarding next generation nuclear reactor designs[1–3] due to its high thermal conductivity, density and melting point, all favourable for enhanced energy production over oxide predecessors. However, for their use, reprocessing and final disposal as spent nuclear fuel (SNF), the understanding of the type and chemistry of formed fission phases is crucial. Based on fuel performance simulations[4,5], it is expected that lanthanide based nitrides (*Ln*N) will form as a prominent constituent. Furthermore, they are expected to form solid solutions with the UN matrix[4–6], which subsequently will affect reactor performance and the behaviour as SNF for final disposal. In conventional UO_2 based fuel, a wealth of knowledge is available regarding *Ln*-O incorporation and interaction with the UO_2 fuel matrix[7–9]. In comparison, far less is known on the interaction and incorporation of *Ln*N phases within UN based fuel, despite the interest around such fuels for next generation nuclear power reactors. Beyond nuclear materials *Ln*N are crucial for recent advances in spintronic devices[10,11], heterogeneous catalysis[12,13], and are relevant for high temperature applications[14,15]. Determining both the solid-state chemical and variable temperature behaviour, particularly oxidation of *Ln*N with, and in addition to UN, is consequently a pertinent endeavour for both next-generation nuclear fuels and advanced functional materials.

UN and all *Ln*N compounds are understood to crystallise in isostructural face- centred cubic structures (rock salt) in the space group $Fm\bar{3}m$[16,17]. With their structural alikeness, they are also highly susceptible to oxidation at ambient conditions, rapidly decomposing after short exposure times to air. This is a key challenge to their potential use and storage as nuclear fuel. In the case of UN, a good foundation of knowledge for the oxidation mechanisms is established[18], whereas *Ln*N with respect to the literature appears largely untouched. It has been shown that UN oxidises at

[1]Institute of Fusion Energy and Nuclear Waste Management (IFN-2), Forschungszentrum Jülich GmbH, Jülich, Germany. [2]Institute for Nuclear Waste Disposal (INE), Karlsruhe Institute of Technology, Karlsruhe, Germany. [3]Institute of Resource Ecology, Helmholtz Zentrum Dresden-Rossendorf, Dresden, Germany. [4]The Rossendorf Beamline at ESRF, The European Synchrotron, Grenoble, Cedex 9, France. [5]Institute for Photon Science and Synchrotron Radiation (IPS), Karlsruhe Institute of Technology (KIT), Karlsruhe, Germany. [6]Institute for Chemical Technology and Polymer Chemistry (ITCP), Karlsruhe Institute of Technology (KIT), Karlsruhe, Germany. [7]Department of Chemistry and Biochemistry, University of Nevada, Las Vegas (UNLV), Las Vegas, NV, USA. [8]Institute of Chemistry and Biochemistry, Freie Universität Berlin, Berlin, Germany. [9]Max-Planck-Institute for Chemical Physics of Solids, Dresden, Germany.
✉e-mail: p.uhlemann@fz-juelich.de; g.murphy@fz-juelich.de

ambient conditions to UO_2 via a so-called *sandwich mechanism*[17], an intermediate structure with separated layers of UO_2 and U_2N_3 that was confirmed via transmission electron microscopy (TEM) in recent studies[19] and also previous[20]. Upon fast heating or at elevated temperatures (> 200 °C), UN will oxidise directly, via ignition, to U_3O_8[21,22]. The oxidation pathway for UN is chemically well studied, and good understanding of the structural basis has been reported[20,22]. In contrast, there is a significant absence of knowledge regarding the oxidation chemistry and mechanisms for *Ln*N at elevated temperatures. Previous Raman spectroscopy measurements have identified in the case of ErN, it proceeds to the sesquioxide, Er_2O_3, at elevated temperatures[16]. Otherwise, the relative rate of oxidation between separate *Ln*N's is not known at ambient or elevated temperatures, nor the behaviour in contrast to UN. It has been shown in the case of UO_2 based fuel and SNF that the chemistry and identity of *Ln* can affect the oxidation resistance and mechanism for UO_2[7]. Particularly, heavier *Ln's* help impede the oxidation onset when occurring within the UO_2 matrix[23]. It is unclear if this trend can be transferred to UN based fuel and SNF materials but is crucial to their potential deployment.

In order to bridge the fundamental gap in knowledge between the chemistry and oxidation behaviour of UN and *Ln*N compounds, this investigation has systematically examined the structure, thermal and redox chemistry of UN and *Ln*N powder compounds for *Ln* = Pr, Nd, Gd, Tb, Dy, Ho, Tm and Lu at room and elevated temperatures. These *Ln*'s were chosen due to their preference to retain trivalent oxidation states and enable a systematic approach to their chemical behaviours with varying ionic radii. Powder X-ray diffraction (PXRD), Dy and Pr L_3-edge high energy resolution fluorescence near edge X-ray spectroscopy measurements (HR-XANES), U L_3-edge XANES in addition to thermogravimetric analysis were performed to understand the evolution of structure, redox and thermal chemistry, respectively at ambient and elevated temperatures. Scanning electron microscopy (SEM) with energy dispersive X-ray spectroscopy (EDS) measurements were performed to assess microstructural changes post oxidation. The work highlights the discord in oxidation behaviour between UN and *Ln*N compounds in following different mechanisms and chemistries. The results of this investigation are discussed in relation to their potential behaviour as a solid solution, and occurrence within UN based SNF.

Results

UN and LnN compound room temperature PXRD structural characterisation

PXRD diffractograms on all collected UN and *Ln*N synthesised phases were analysed using the Rietveld method where consistent cubic structures in space group $Fm\bar{3}m$, consistent with cubic face-centred rock salt structures, could be refined against the data. Figure 1 provides the Rietveld profiles for all investigated compounds, whereas Table 1 provides the refined lattice parameters and structural data. It was found that compared to literature values, the results are largely in agreement with small deviations attributed to non-stoichiometry in nitrogen content. In the case of UN, inspection of the diffraction data showed the subtle splitting of peaks consistent with phase separation between a main UN and secondary slightly oxidised UN phase. Accordingly, a 2-phase refinement was performed against this diffractogram with determined lattice parameters of 4.89550(4) and 4.907885(21) Å. When considering the reference data on UN from Liu et al.,[24] which provides a lattice parameter of $a = 4.8914(1)$ Å, both of these phases possess slightly larger lattice parameters. Nevertheless, comparing the value obtained in this study with Liu et al. and literature, the synthesized sample can be considered of strong purity and two phase assemblage attributed to subtle differences in nitrogen stoichiometry[25,26]. Slight Ta_2N and NbN impurities were observed in the *Ln*N analysis, which are attributed to the experimental set up used in the synthesis. Their maximum amount was determined to be less than 0.7 and 1.9 wt%, respectively.

The cubic face-centred structures of the UN and *Ln*N compounds is graphically represented in Fig. 2a. The structures consist of the central U/*Ln* cations, which are six-fold coordinated by surrounding nitrogen atoms, that are themselves also six-fold coordinated. The U/*Ln* environment is high symmetry, with equal bond lengths with all nitrogen atoms.

Figure 3 plots the determined lattice parameters of the pristine nitride compounds as a function of the ionic radii of the *Ln* or U cations[27]. From the Figure, a linear trend for all *Ln*N compounds is clearly observed involving gradual lattice contraction with heavier *Ln* present, consistent with the known lanthanide contraction. However, when the lattice parameter value and ionic radius for U^{3+} in UN are considered in this figure[27,28], it does not display linear behaviour compared to the *Ln*N compounds, despite being isostructural. Linear behaviour would be indicative of classical Vegard's law like behaviour as solid solution, which is not supported by this data. Similar aberrations are noted for CeN, which has a reported lattice parameter of $a = 5.022$ Å, if plotted against the Shannon ionic radii of Ce^{3+}, see Fig. 3[27,29]. That it does not possess similar behaviour to other *Ln*N compounds was attributed to variability in its valence state and electronic structure[30,31], deviating away from a pure Ce^{3+} state. Such behaviour could also be present for UN, considering the noted instability of the U^{3+} cation and heightened stability when accessing the U^{4+} state.

Room temperature oxidation studies

It has been previously noted that the oxidation tendency for *Ln*-doped UO_2 materials is dependent upon the type and amount of *Ln* present, whereby heavier *Ln*'s inhibit oxidation as opposed to lighter *Ln*'s, which allow it to proceed[7]. To examine whether this chemical effect and trend is potentially present for the pure UN and *Ln*N compounds, room temperature oxidation studies were performed. To ensure physical comparability between the samples, powders with particle size < 100 µm were used. These measurements, involving precise tracking and weight change monitoring of materials as they oxidized over a 10 min period when exposed to ambient conditions, were analysed via regression analysis (Supplementary Information Note 1, Fig. S1 and Table S1). It was found that the oxidation process followed relatively linear behavior in this time frame such that the rate of mass from oxidation ($\nu_{10\,min}$, (µg min^{-1})) could be determined by regression analysis where an associated linear fit was used as approximation. Values determined are provided in Table 2 and plotted as a function of U/*Ln* ionic radii[27,28] in Fig. 4.

From Fig. 4, *Ln*'s with larger ionic radii were found to exhibit relatively fast oxidation in contrast to *Ln*'s with smaller ionic radii which oxidise much more slowly. Furthermore, the *Ln*'s with smaller ionic radii appear to exhibit more similar behaviour, asymptotically, contrasting to the larger *Ln*'s. This behaviour is reminiscent of the effect *Ln's* have upon the variable rate of oxidation of UO_2[23]. In the case of UN from Fig. 4 it shows contrasting behaviour to the *Ln*N compounds and does not appear to show a correlating trend. Interestingly, its behaviour in Fig. 4 is highly reminiscent of that observed in Fig. 3 regarding the lattice parameter behaviour as a function of ionic radii. These results would imply there is contrasting chemistry both structurally and regarding oxidation between the UN and the *Ln*N's. Notably, the results of this study apply to the investigated trivalent Ln^{+3} nitrides, which oxidise consistent to trivalent oxides. In the case of CeN, which can access trivalent and tetravalent Ce upon oxidation, it has been shown when exposed to air forms rapidly CeO_2 rather than hydroxide[32]. This indicates a more complex oxidation mechanism and hints at the effect of redox of the *Ln* cations, particularly when able to access multiple different oxidation states, on oxidation pathway that has not been examined in the present study.

The room temperature oxidised nitrides obtained after the isothermal gravimetric analysis were analysed via PXRD and Rietveld analysis in order to determine the structural changes. Air exposure of the nitride powders leads to rapid oxidation within one hour and full conversion to the complete oxidized product can be observed within a day for *Ln*'s with larger ionic radii and within 3 days for *Ln*'s with smaller ionic radii. During the oxidation the powders undergo a color change from black to light green for PrN, black to light violet for NdN, black to light pink for HoN and black to white for the other, as well as a distinguishable volume expansion. The change in sample

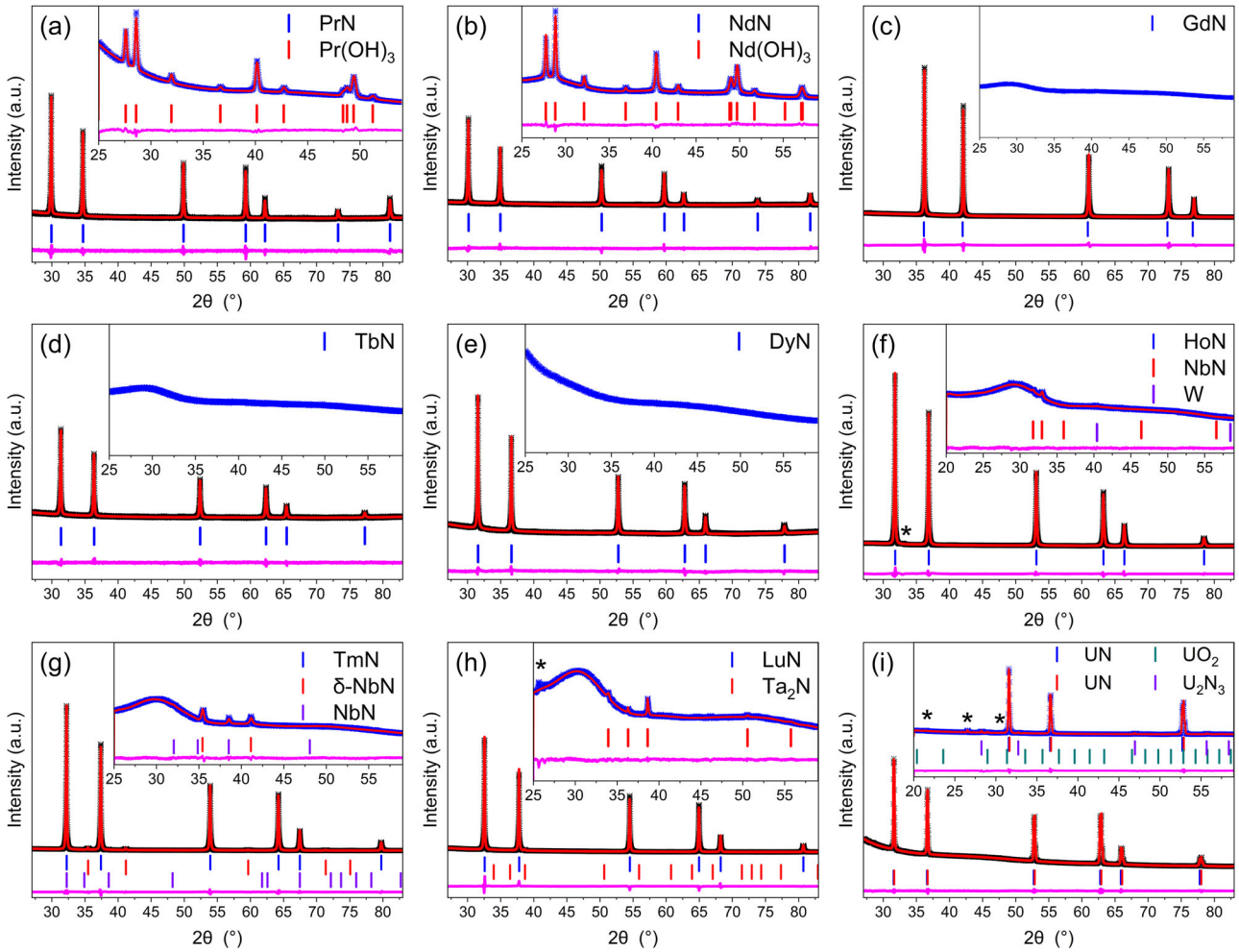

Fig. 1 | Pre- and post-oxidation PXRD comparison of investigated LnN/UN samples. Rietveld profiles made against PXRD data of pristine *Ln*N (*Ln* = Pr (**a**), Nd (**b**), Gd (**c**), Tb (**d**), Dy (**e**), Ho (**f**), Tm (**g**), Lu (**h**)) and UN (**i**) phases. The insets provide corresponding Rietveld profiles for the same samples oxidised in air at room temperature. The black and blue crosses correspond to collected data for the pre- and post-oxidised samples. The red and pink lines correspond to the calculated and difference profiles. The blue, red and violet markers correspond to the allowed reflections according to the space groups of respectively UN and *Ln*N crystallising in $Fm\bar{3}m$ cubic face-centred structure, oxidised nitride phases $Pr(OH)_3$, $Nd(OH)_3$ crystallising in hexagonal $P63/m$ structure, and UO_2/U_2N_3 respectively crystallising in $Fm\bar{3}m$ and $Ia\bar{3}$ structure. Reflexes arising from Vaseline used to fixate the powders were marked in (**f**), (**h**) and (**i**) with black stars.

appearance during the RT oxidation is example wise shown on photos for NdN in Fig. 5.

From the Rietveld analysis, provided in the insets of Fig. 1, it was found the PrN and NdN phases consistently transformed into the crystalline hydroxide phase, $Ln(OH)_3$ with hexagonal structures in space group $P63/m$ (176). A structural representation of the structure is provided in Fig. 2b and refinement details are provided in Table 3. In the case of Gd, Tb, Dy, Ho, Tm and Lu nitrides, these compounds were found to adopt amorphous structures. Nevertheless, based on the consistent oxidation behaviour and SEM analysis, discussed in the subsequent sections, they were consistent with hydroxide phase formation.

In comparison to the *Ln*N compounds, UN was found to undergo a considerably different oxidation structural pathway at ambient conditions. Oxidised UN was found to adopt a dual phase material consistent of U_2N_3 and UO_2, which is in accordance with its oxidation mechanism previously described[17]. Previous studies[19,33,34] have identified the formation of a thin adherent layer of UO_2 passivating the surface of the bulk UN. The formed U_2N_3 and UO_2 phases both crystallise in cubic structures of respectively a C-type bixbyite (space group $Ia\bar{3}$) and cubic fluorite (space group $Fm\bar{3}m$). Structural representations for these are provided in Fig. 2c, d. Although binary LnO_2 oxides are not expected for the investigated *Ln*N compounds upon oxidation to air owing to the stability of the Ln^{3+} oxidation state in oxide form, some of these can adopt similar sesquioxide type C-type bixbyite Ln_2O_3[8]. However, there appear to be no reports of this formula forming in the nitride case, Ln_2N_3, as is observed like forUN with U_2N_3. Moreover, the PXRD analysis upon oxidation under ambient conditions of *Ln*N and UN compounds shows a discord between the structural behaviour of these. Consequently, the results suggest as mixed compounds, the oxidised phases are immiscible in each other. Critically, it suggests the oxidation mechanisms are inherently chemically different in which the *Ln*N compounds proceed under the presence of moisture or humidity (H_2O) via a hydrolysis mechanism, resulting in the formation of hydroxide phases. Contrastingly, UN oxidises via the presence of O_2 and not through H_2O.

The PXRD measurements of ambient condition oxidised UN and *Ln*N compounds revealed that they adopt incongruent structure types of mixed oxide/nitride for UN and hydroxide and amorphous for the *Ln*Ns. In order to investigate whether this dissimilar behaviour occurs not just structurally, but also microstructurally, SEM measurements were performed. In Fig. 6 SEM-BSE images of the *Ln*N oxidised at ambient conditions are compared. From inspection of the images, they were found to adopt very similar morphologies upon air exposure where consistent flaky microstructures are adopted. One-directional layers of sheets appear to be located within the flaky regions, which are caused by the volume expanding nature of the oxidation process. Additional SEM-EDS spot

Table 1 | Refined lattice parameters determined from Rietveld refinements against PXRD data, associated fitting factors and literature lattice parameters for pristine UN and *Ln*N (*Ln* = Pr, Nd, Gd, Tb, Dy, Ho, Tm, Lu) phases

Compound	Structure and space group	Lattice parameter (Å)	Fitting factors	Reference lattice parameter (Å)
PrN	Cubic face- centred $Fm\bar{3}m$	a =5.165461(23)	R = 3.63 % R_w = 4.57 %	a = 5.1690[55]
NdN		a = 5.129534(21)	R = 3.57 % R_w = 4.55 %	a = 5.132[56]
GdN		a = 4.989627(10)	R = 3.73 % R_w = 4.74 %	a = 4.978[56]
TbN		a = 4.934947(22)	R = 2.46 % R_w = 3.19 %	a = 4.9344(10)[57]
DyN		a = 4.902536(17)	R = 1.46 % R_w = 1.95 %	a = 4.9044(7)[57]
HoN		a = 4.871501(11)	R = 2.96 % R_w = 4.33 %	a = 4.8732(7)[57]
TmN		a = 4.805925(9)	R = 3.10 % R_w = 4.30 %	a = 4.8021(4)[57]
LuN		a = 4.758154(10)	R = 2.81 % R_w = 4.10 %	a = 4.7599(4) [57]
UN		a = 4.89550(4) (35.40 wt%) 4.907885(21) (64.60 wt%)	R = 1.19 % R_w = 1.65 %	a = 4.8914(1) [24]

Additional refinement details are shown in Supplementary Information Note 2, Table S2. Note uncertainties are reported directly from the Rietveld analysis with no correction.

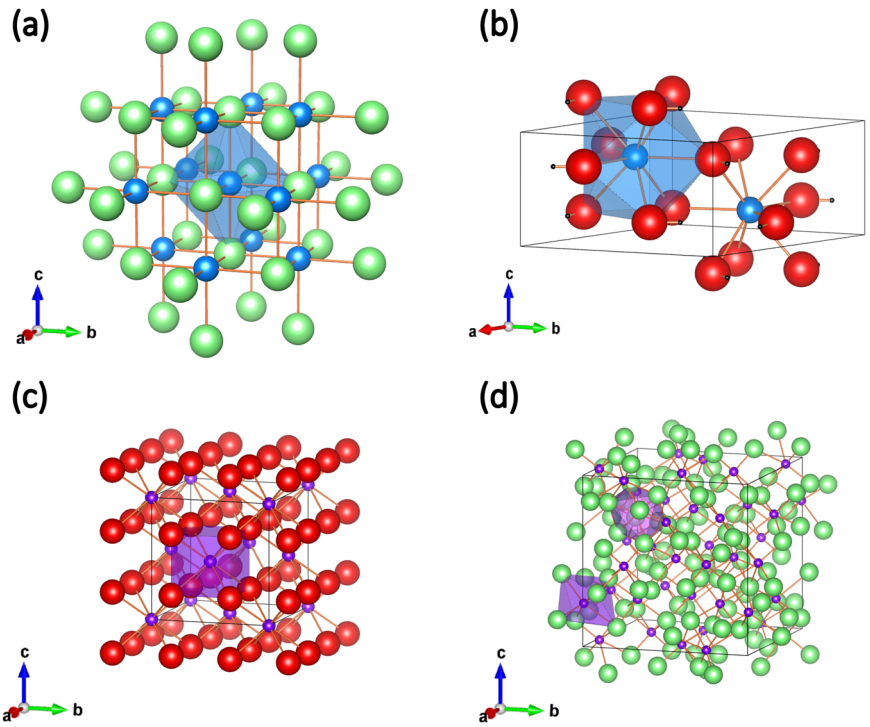

Fig. 2 | Crystal structures of *Ln*N/UN and their oxidation products. a General structural representation of the face-centred cubic structures in space group $Fm\bar{3}m$ for *Ln*N/UN (*Ln* = Pr, Nd, Gd, Tb, Dy, Ho, Tm, Lu), and structural presentation of (**b**) hexagonal $Ln(OH)_3$ in space group $P63/m$ (**c**) cubic fluorite UO_2 in space group $Fm\bar{3}m$ and (**d**) cubic U_2N_3 in space group $Ia\bar{3}$ which are identified as crystalline structural oxidation products for *Ln*N and UN compounds determined from this investigation. The red atoms represent oxygen, green atoms nitrogen, blue atoms lanthanides, violet atoms uranium and black atoms hydrogen.

measurements were further conducted (Supplementary Information Note 3, Figs. S2, S3, S4, S5, S6, S7 and S8) indicate the near complete loss of nitrogen. Consequently, with the results of the PXRD and SEM analysis so far, the room temperature oxidation of *Ln*N compounds to oxidised products can be described according to Eq. 1, namely a hydrolysis reaction for oxidation. Note this is further argued for the amorphous phases, which is discussed in more depth in subsequent XANES sections.

$$2LnN + 6H_2O \rightarrow 2Ln(OH)_3 + 2NH_3 \quad (1)$$

Figure 7 provides SEM-EDS measurements of UN oxidised under ambient conditions. Contrasting to Fig. 6 and the *Ln*N compounds, the oxidised UN adopts a more complex morphological microstructure where some parts, although minor, are found to possess the flaky structure also identified for *Ln*N, in addition to structure which is reminiscent of the UO_2 microstructural morphology[35]. EDS spectra collected on the U-M, N-K and O-K edges as provided in Fig. 7 highlights some oxygen hot spots, however these are assigned to impurities. The EDS spectra indicates passivation from oxidation as shown by the consistent stronger signal

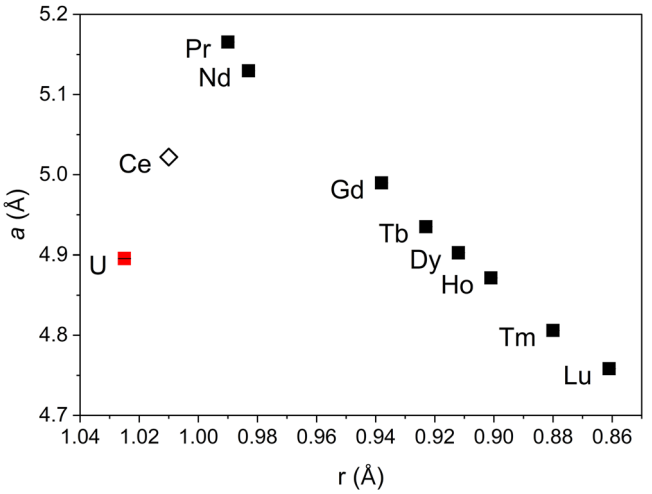

Fig. 3 | Lattice parameters as a function of ionic radii for the investigated UN and *Ln*N compounds. Lattice parameters as a function of ionic radii for the investigated UN and *Ln*N compounds investigated based on their reported associated cation ionic radius[27,28] when in a trivalent 6-fold coordinated environment. Additionally, CeN is plotted as reference from literature values[29].

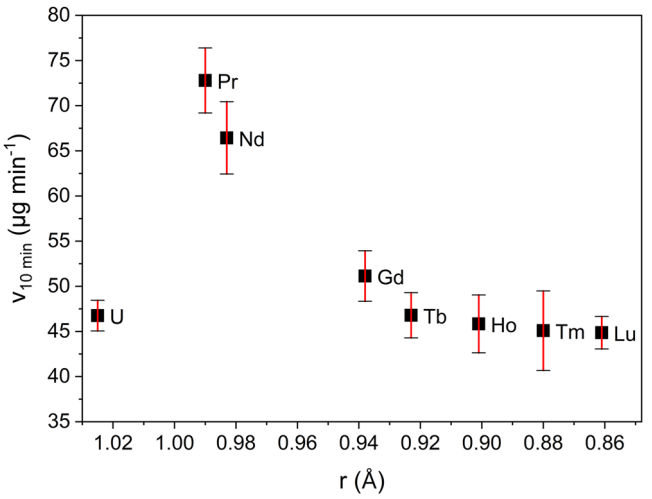

Fig. 4 | Oxidation rates of *Ln*N (*Ln* = Pr, Nd, Gd, Tb, Ho, Tm, Lu) powders. Oxidation rates of *Ln*N (*Ln* = Pr, Nd, Gd, Tb, Ho, Tm, Lu) powders with < 100 µm particle size exposed to air for 10 min as function of their associated cation ionic radius, based on their reported ionic radii[27] when in a trivalent 6-fold coordination environment.

arising from the N-K over O-K edge. Consistent with the XRD analysis, this shows that the room temperature oxidation of UN results in superficial oxidation via the adoption of diphasic chemical species, namely UO_2 and U_2N_3 which contrast the behaviour of oxidised *Ln*N. The formation of U_2N_3 with simultaneous occurrence of UO_2 seems contradicting, although it aligns with the observation made in previous works[17,20,21]. Following the oxidation mechanism proposed by Dell and coworkers[17] provided in Eqs. 2 to 7, the formation of U_2N_3 is the result of liberated nitrogen reacting with bulk UN (Eq. 3). This nitrogen originates from the initial surface oxidation of the UN (Eq. 2) and is described to become trapped in the lattice interstitially. Additionally, the presence of interstitial nitrogen promotes the formation of the hyperstoichiometric U_2N_{3+y} (Eq. 6), which is instable in contact with oxygen from UO_2 at the U_2N_3 – UO_2 interface and oxidises as shown in Eq. 7. This behaviour establishes a chemical gradient which causes oxygen to diffuse from the oxygen rich UO_{2+x} surface (Eq. 5) through the UO_2 layer to the U_2N_3–UO_2 interface,

Table 2 | Oxidation rates for *Ln*N (*Ln* = Pr, Nd, Gd, Tb, Dy, Ho, Tm, Lu) and UN powders with < 100 µm particle size exposed to air for 10 min

Compound	$v_{10\,min}$ (µg min^{-1})
PrN	72.80(36)
NdN	66.40(4)
GdN	51.10(28)
TbN	46.80(25)
HoN	45.80(32)
TmN	45.10(44)
LuN	44.90(18)
UN	46.80(17)

The uncertainty is given as 2σ resulting from the standard error of the applied linear regression, see Supplementary Information Note 1, Fig. S1 and Table S1.

where the U_2N_3 is consumed to form UO_2 driving the oxidation of the material from the surface inwards to the bulk material.

$$UN(s) + O_2(g) \rightarrow UO_2 + N_{interstitial} \quad (2)$$

$$2UN(s) + N_{interstitial} \rightarrow U_2N_3(s) \quad (3)$$

$$N_{interstitial} + N_{interstitial} \rightarrow N_2(g) \quad (4)$$

$$UO_2(s) + xO_2(g) \rightarrow UO_{2+x}(s) \quad (5)$$

$$U_2N_3(s) + yN_{interstitial} \rightarrow U_2N_{3+y}(s) \quad (6)$$

$$U_2N_{3+y}(s) + 2O_2(s) \rightarrow 2UO_2(s) + (3+y)N_{interstitial} \quad (7)$$

To shed further light on the changes to redox chemistry of the oxidised UN and *Ln*N phases, U L_3-edge XANES of UN and *Ln* L_3-edge HR-XANES of DyN and PrN were performed. Pristine nitride compounds were investigated in addition to partially (LnN_{ox}) and fully (LnN_{fox}, *Ln* = Pr, Dy) oxidised samples along with selected references. In the case of UN, the near pristine sample could not be measured due to logistical issues of radioactive transport and instead a slightly oxidised sample containing 6.4 wt % UO_2 and 1.2 wt % U_2N_3 was investigated (see Supplementary Information Note 4, Figs. S11 and S12). Whereas DyN and PrN were found to completely oxidise to $Dy(OH)_3$ and $Pr(OH)_3$, the UN was found to adopt a phase assemblage of UO_2 and U_2N_3 (see Supplementary Information Note 5, Figs. S13, S14 and S15). The normalised XANES/HR-XANES data for all compounds and references are provided in Fig. 8.

In the case of PrN and DyN, the use of HR-XANES enables better energy resolved measurement of pre-edge and post edge features as compared to conventional XANES. We find that the position of the most intense peak, the white line (WL), of the Pr and Dy L_3 edge HR-XANES spectra does not shift upon air exposure. It appears at a similar energy as for $Pr^{3+}Cl_3$ and $Dy^{3+}{}_2O_3$ references, suggesting a retention of the trivalent oxidation state of $Pr^{3+}N$ and $Dy^{3+}N$ before and after air exposure. Variations between the spectra of *Ln*N, LnN_{ox} and LnN_{fox} are found in the shape of the WL as well as the pre- and post-edge regions located at lower and higher energies than the WL, respectively. The post-edge region is largely influenced by interference patterns resulting from scattering paths involving the atoms surrounding the central atom and differences are therefore indicative of differing local atomic environments. The pre-edge in the *Ln* L_3-edge spectra is predominantly a result of (weak) quadrupole transitions into unoccupied *Ln* 4f-dominated molecular orbitals. The lack of local inversion symmetry leads to mixing of the 4 f

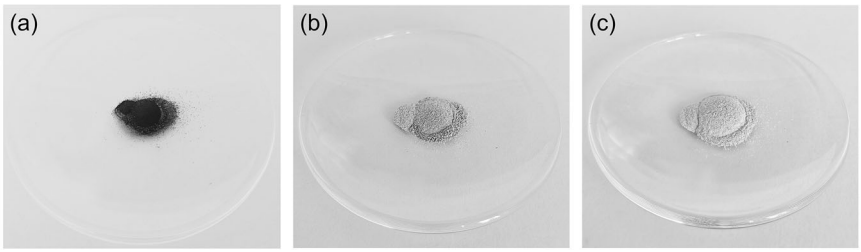

Fig. 5 | Visualisation of *Ln*N oxidation at ambient conditions. Photos of NdN oxidation at RT in air with **(a)** pristine NdN, **(b)** after 1 h, and **c** after 24 h in air.

Table 3 | Summary of determined crystalline phases resulting from the oxidation of *Ln*N (*Ln* = Pr, Nd) and UN in air via Rietveld analysis and their respective literature lattice parameters

Compound	Oxidised Phase	Structure and Space Group	Lattice Parameters (Å)	Fitting factors	Literature lattice parameter (Å)
PrN	$Pr(OH)_3$	*P*63/*m* (176)	*a* = 6.4669(9) *c* = 3.7616(1)	R = 1.29% R_w = 1.75%	*a* = 6.456(1) *c* = 3.769(1)[58]
NdN	$Nd(OH)_3$	*P*63/*m* (176)	*a* = 6.4394(7) *c* = 3.7298(1)	R = 1.21% R_w = 1.59%	*a* = 6.418(2) *c* = 3.743(1)[59]
UN	UO_2	$Fm\bar{3}m$ (225)	*a* = 5.4727(5) (2.01 wt%)	R = 2.82% R_w = 4.04%	*a* = 5.468(1)[60]
	U_2N_3	$Ia\bar{3}$ (206)	*a* = 10.6754(2) (0.81 wt%)		*a* = 10.685(2)[61]
	UN	$Fm\bar{3}m$ (225)	*a* = 4.8940(1) (39.90 wt%) 4.909(21) (57.28 wt%)		*a* = 4.8914(1)[24]

Additional refinement results provided by Rietveld analysis shown in Supplementary Information Note 2, Table S2.

and 5 d states, thereby introducing also contributions from dipole transitions in this spectral region.

In contrast, the main absorption edge results from transitions into unoccupied 5d-dominated molecular orbitals, which are dipole allowed and therefore much more intense. The energy difference between the absorption edge, defined as the first inflection point determined by the maximum of the first derivative of the spectrum, and the maximum of the pre-edge (ΔE(*5 d,4 f*)) has been established as a measure of covalent contributions to bonding in previous work[36]. A larger ΔE value indicates increased *Ln*-ligand bond ionicity. In the spectra measured for both lanthanides, this value increases after air exposure, following the change from a nitrogen- to an oxygen-based *Ln* bond (see Supplementary Information Note 5, Table S3).

For the Pr sample set, this value increases linearly as the WL shape changes from broad with a soft pre-edge to two well-separated and comparatively sharp features (see Supplementary Information Note 5, Fig. S13). There is a clear shift in the absorption edge position towards higher energies and a parallel increase in intensity, while the pre-edge feature only changes in its identifiability. The shape resonances in the post-edge shift slightly but systematically to lower energies, indicating a change in local atomic structure. A similar overall behaviour is observed for the Dy sample set (see Supplementary Information Note 5, Fig. S14): The sharpening of the WL during oxidation appears and ΔE(*5 d,4 f*) increases. However, this increase is smaller between DyN and DyN_{fox} (0.8 eV) than between PrN and PrN_{fox} (1.4 eV). An obvious change in the underlying features that make up the WL, with a shoulder appearing in the WL of DyN_{fox} is also observed. A feature in this region is most likely due to splitting of the unoccupied 5*d*-dominated states. It is unclear whether this feature is present and simply invisible under the broader WL of PrN or if it is not present at all. The differences could be explained by a change in crystal structure and resulting change in crystal field splitting. Such deeper focus is beyond the scope of the present study.

The post-edge features of the PrN and DyN spectra, which are caused by scattering at the nearest neighbors in the crystal structure, have similar shapes in agreement with the PXRD results that the compounds have the same crystal structure (Supplementary Information Note 5, see Fig. S15). Similar changes of the post-edge features for PrN_{ox} and DyN_{ox} are observed compared to the spectrum of the respective nitride compounds. This suggests a similar structural change for both compounds and supports the proposition that the amorphous phase observed for DyN, and for other amorphous oxidized *Ln*N compounds after exposure to ambient conditions, is indeed hydroxide based. $PrCl_3$ and Dy_2O_3 exhibit very different post-edge features, which supports this argument. Consequently, it is argued that the ambient condition oxidation of *Ln*N compounds involves hydrolysis given by Eq. 1.

Generally, ΔE(*5 d,4 f*) points to an increase in ionicity that can be well explained by the change from nitrogen- to oxygen-based bonds in the material. It is evident that no change in oxidation state takes place for these materials upon air exposure, though changes in crystal structure, as evidenced by the post-edge development, electronic structure and bonding properties are clearly visible.

For UN, regular XANES experiments found the oxidation to result in a small shift to higher energy. Consistent with the PXRD analysis, this indicates an oxidation state change from U^{3+} to U^{4+}. It has been previously described that compared to UO_2, the electronic structure of UN is considerably more covalent. This description has been previously discussed by Gouder and coworkers[37]. Moreover, the XANES analysis for the investigated compounds indicates that upon oxidation for PrN and DyN the *Ln* cations are contained within their trivalent states, and it is expected this will be encountered for other Ln^{3+}N compounds considered in this investigation, considering their stable trivalent redox chemistry. Contrastingly, UN involves a more complex redox mechanism involving the occurrence of both U^{4+} and U^{3+} with oxidation, attributed to the respective formation of UO_2 and U_2N_3.

High temperature oxidation studies

In the context of SNF materials and indeed other elevated temperature applications, it is important to consider the high temperature induced oxidation of UN and *Ln*N compounds investigated in the presented manuscript. TGA-DSC measurements were subsequently recorded on all

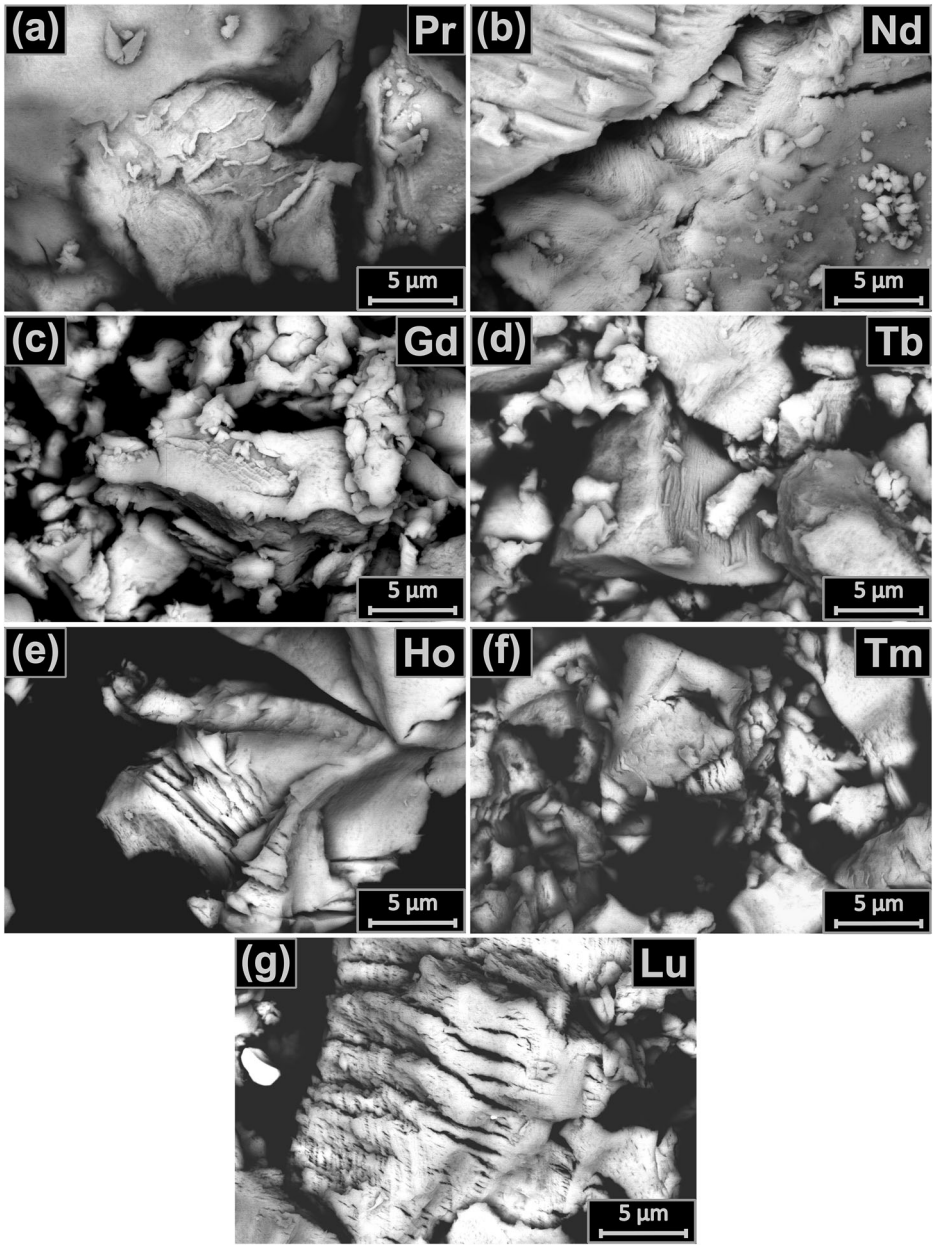

Fig. 6 | SEM-BSE images of investigated air oxidised LnN samples. SEM-BSE images of $Ln(OH)_3$ (*Ln* = Pr (**a**), Nd (**b**), Gd (**c**), Tb (**d**), Ho (**e**), Tm (**f**), Lu (**g**)) powders received by oxidation at ambient conditions of their respective *Ln*N powders < 100 µm particle size in air, showing fibrous microstructures for all investigated powders.

materials under consistent conditions, in which their combined TGA results when heated from RT to 900 °C are provided in Fig. 9. The TGA was normalized against the fully oxidised end member products that were recovered after the samples were cooled to room temperature. This was done, since some *Ln* oxides exhibit varying stoichiometries at higher temperature, even when heated in oxidising conditions. Details regarding specific TGA-DSC measurements and associated post PXRD analysis are provided in Supplementary Information Note 6, Figs. S16–S27. Individual TGA-DSC profiles are provided in Supplementary Information Note 6, Figs. S16–S18. It was found a relative trend can be observed where upon the onset temperature of oxidation, T_{onset}, defined as 5% of total mass change of the nitride to oxide reaction, followed a relatively linear trend for the lanthanides as a function of their ionic radii as plotted in Fig. 10. Full details of the TGA-DSC results, including determined formed phases as identified via PXRD analysis are provided in Table 4. Individual PXRD analyses of the oxidised phases are provided in Supplementary Information Note 6, Figs. S19–S27 with determined refinement values in Table S4.

The oxidation behaviour of specific *Ln*'s was found to follow, at times, different intermediates for instance the occurrence of $PrO_{1.70}$ at 900 °C which when cooled adopted $PrO_{1.84}$. Comparatively, GdN oxidised to $GdO_{1.50}$ (~ Gd_2O_3) at 900 °C and cooled to the same formula. The difference in high temperature behaviour is attributed to the variability in their redox chemistry in oxide state at high temperature. During the whole runs of all the nitrides after the transition to the oxides, slight mass variations can be observed (Supplementary Information Note 6, Figs. S16–S18), which are attributed to loss of oxygen specifically observed in the 30 min hold at 900 °C with details provided by the insets of Figs. S16–S18.

In the case of UN, this was found to oxidise directly to UO_3 followed by transformation to U_3O_8, this behaviour is consistent with literature[22]. Notably, the U_2N_3 intermediate was not observed from TGA measurements. Likely, the nitrogen, from Eqs. 2 and 3 has been rapidly liberated as the UN is quickly oxidised to oxide form. Critically, this suggests at room temperature and variable temperature, UN oxidises under a consistent mechanism, as previously demonstrated in this investigation, mediated via atmospheric O_2. Compartively, *Ln*N compounds have variable mechanisms, at room temperature oxidation is induced via hydrolysis and access to atmospheric H_2O as opposed to high temperature in dry atmospheres which is directly via oxygen.

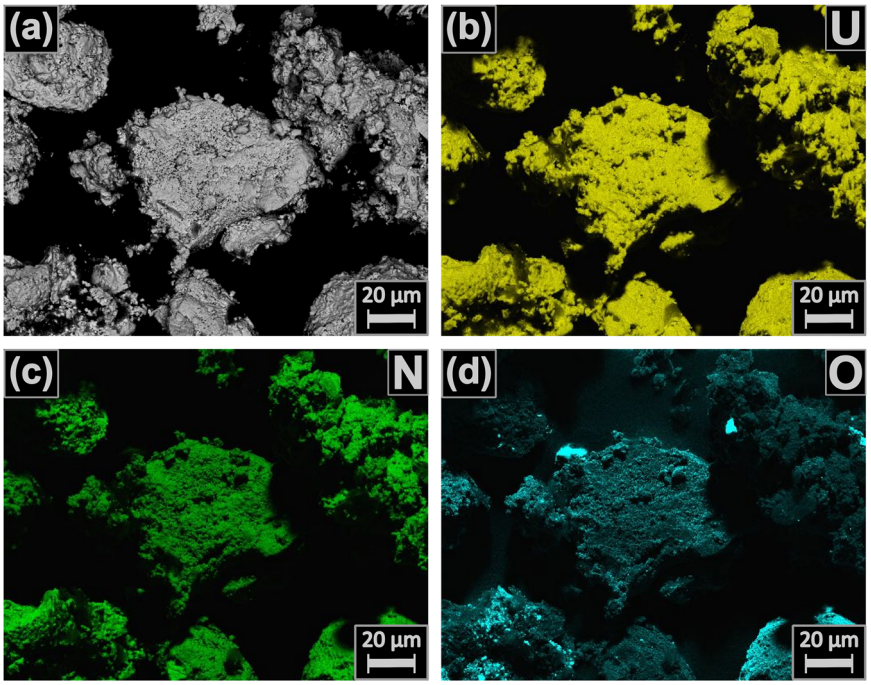

Fig. 7 | SEM-EDS elemental maps of oxidised UN. SEM-EDS elemental maps of oxidised UN (**a**) BSE image (**b**) U-M map (**c**), N-K map (**d**) and O-K map. High intensity O spots correlate with impurities (cross contamination), for further details check Supplementary Note 2, Figs. S9 and S10.

A pertinent observation is the relatively linear trend for the T_{onset} for all examined compounds with the size of U/*Ln* cation considered (Fig. 10). Particularly, UN and PrN oxidise at the lowest temperatures, but as the size of *Ln* cation decreases, the T_{onset} increases, with LuN oxidising at the highest temperature. These observations are similar to that described for the room temperature studies described previously, where the oxidation rate was found to be more inhibited with heavier or smaller *Ln* cations. Noticably, between the T_{onset} of GdN and TbN a break in the trend can be observed, that separates the trend of T_{onset} in two groups of one group with *Ln* = Pr, Nd, Gd and the second with *Ln* = Tb, Dy, Ho, Tm, Lu. This break is consistent with the lanthanide tetrad effect, specifically between the 2nd and 3rd tetrad break that corresponds to the half-filling of the 4f-orbitals[38].

Oxidation of UN and *Ln*N compounds in relation to UN spent fuel

The results of the investigation thus far have provided an in-depth investigation into the contrasting room and high temperature oxidation of *Ln*N and UN compounds. Considering the relevance of these compounds to UN derived SNF, it is important to discuss their associated chemistry, specifically differences in reactivity, and potential associated implications.

As part of this investigation, it was shown that *Ln*N compounds exhibit different oxidation reactivities at ambient and high temperatures, which is reminiscent of the two-stage mechanism kinetics described for the hydroxylation of La_2O_3, where a slow initial adsorption-controlled surface reaction is followed by a transition to rapid bulk reaction once a critical surface expansion is reached[39]. A preferred hydrolysis via water in the initial reaction step indicates that the activation energy for oxygen adsorption and the subsequent oxidation is higher than for water. Similar oxidation tendency was found for the oxidation of UN at high temperatures[40]. However, consistent with literature, contact of combined oxygen and water at ambient or high-temperatures results in the formation of uranium oxide species[41], as described by a well-established oxidation mechanism for UN[17]. Similar reactivity was observed as mentioned for CeN, forming oxide products at ambient temperatures[32]. It correspondingly suggests the importance of redox in influencing reactivity and rate towards thermodynamically stable products from oxidation.

As SNF, a paucity of information remains regarding the chemistry of spent UN fuel in open literature, largely due to the relatively recent interest and consideration for UN in nuclear energy production. From simulations, the generation of *Ln* fission products is expected to result in a larger proportion 2.74 mol% at 60 $MWd{\cdot}kg^{-1}$ burnup after one year of cooling[4], from the expected fission product pool where they are soluble in the UN structure[4,5]. Although this investigation did not examine the solid solution behaviour of *Ln's* in UN, previous works demonstrate solid solution behaviour occurs readily[6,42–46]. This solid solution behaviour is readily rationalised via the close structural relationship between UN and *Ln*N phases as isostructural compounds, as shown in this work and elsewhere[6,42–46]. Accordingly, during *in-pile* irradiation, a solid solution of *Ln*'s within UN is expected, as graphically illustrated in Fig. 11a and confirmed by post-irradiation studies[44,47].

It is pertinent to consider how a solid solution of *Ln*-doped UN may oxidise or as end member phases in the context of UN SNF. After *in-pile* irradiation, UN SNF is expected to remain hot at the surface of the fuel with temperatures above ambient. Unexpected breach of the cladding may result in rapid oxidation of the fuel matrix, as shown by the high temperature studies performed in the present investigation. Such an event could occur during a loss of cooling accident (LOCA) during *in pile* irradiation or post irradiation cooling and assembly transfer. *Ln*-doped UN would be expected to rapidly evolve to higher oxide structures. The formation of sesquioxide *Ln* phases would be expected to be soluble within a UO_2 matrix or within U_3O_8 (but less so comparatively)[7], nevertheless, they would be expected to be retained considering expected fission product amounts. At the same time, the present study has identified that heavier or smaller *Ln* cations exhibit reduced oxidation rates at elevated temperatures. Similar behaviour has been observed for *Ln*-doped UO_2[7]. This consequently suggests that the inclusion of *Ln*'s, particularly heavier ones, will inhibit the high temperature oxidation tendency of the UN matrix, stabilising it. This is subsequently a relatively beneficial effect if UN fuel is used as a part of fast reactors that use high burn up cycles. A graphical representation illustrating this effect on the microstructure is provided in Fig. 11c for this scenario of elevated temperature.

After sufficient cooling, spent UN fuel can be subject to long term storage, such is what is intended for many UO_2 and MOX based fuels in many countries, where the fuel is expected to be exposed to ambient temperatures. Depending on the environment surrounding the UN SNF, it can be subject to atmospheric wet oxidation conditions. From the results of this investigation, it strongly suggests *Ln*-doped UO_2 would be subject to phase

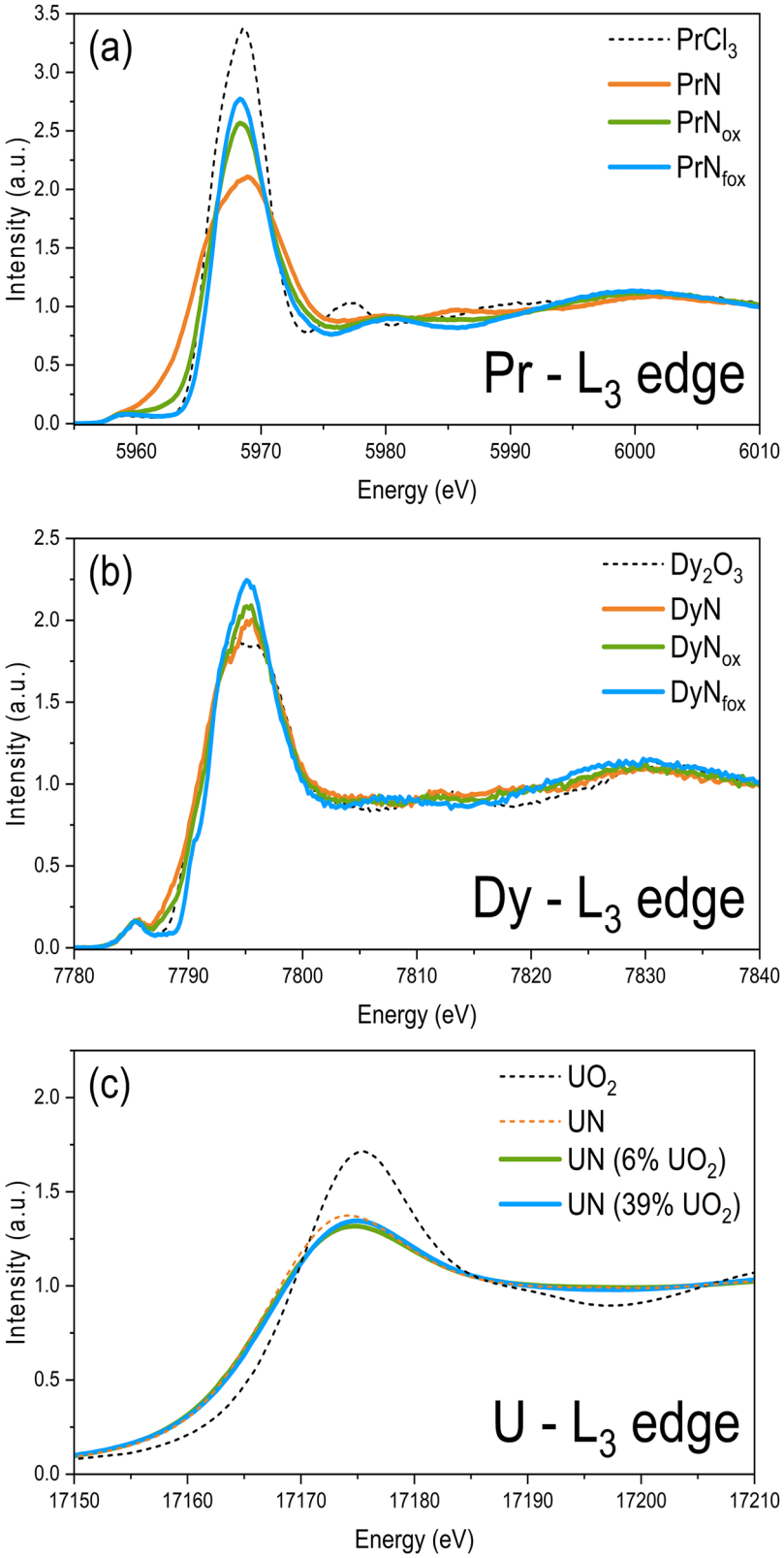

Fig. 8 | HR-XANES spectra of selected LnN/UN and its oxidation products. HR-XANES spectra (normalised to edge jump 1) of (**a**) at the Pr L_3-edge for PrN, partially (ox) and full oxidised (fox) PrN samples with $Pr^{+3}Cl_3$ reference; (**b**) at the Dy L_3-edge for DyN, partially (ox) and full oxidised (fox) DyN samples with $Dy_2{}^{+3}O_3$ reference; (**c**) U L_3-edge XANES spectra for UN samples containing 6.4 wt %/1.2 wt% and 38.8 wt%/1.5 wt% UO_2/U_2N_3, and UO_2 and UN reference; respectively measured on the cation L_3-edge.

separation with the formation of U_2N_3, UO_2 and $Ln(OH)_3$ species, of which the *Ln*'s are not expected to be readily soluble in the U compounds. At the microstructural scale, this would involve phase separation of materials and is graphically illustrated in Fig. 11b. Notably, such conditions are generally avoided in a geological repository by ensuring anaerobic conditions through container materials. However, they can also be released through ground water intrusion and radiolysis. Similarly, in an interim storage scenario, anaerobic conditions are not guaranteed. Notably, some studies have examined the oxidation of UN under conditions of high temperature steam, identifying oxidation products[24]. Considering the thermodynamic stability of hydroxide phases compared to oxides, despite the chemical potential for $Ln(OH)_3$ phases to occur under such conditions, thermodynamically oxides

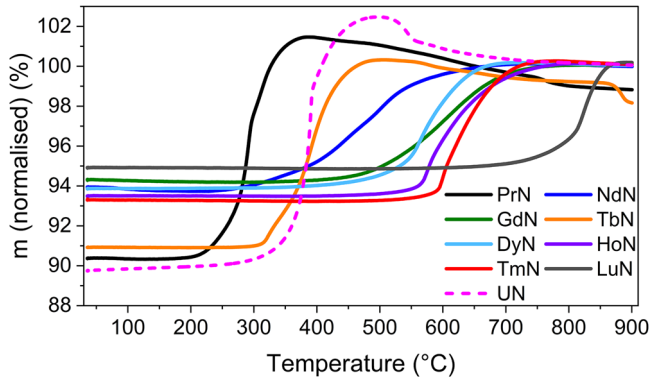

Fig. 9 | TGA profiles for investigated *Ln*N (*Ln* = Pr, Nd, Gd, Tb, Dy, Ho, Tm, Lu) and UN. TGA profiles for investigated *Ln*N (*Ln* = Pr, Nd, Gd, Tb, Dy, Ho, Tm, Lu) and UN samples heated to 900 °C in synthetic air, normalised to the endpoint of the measurements.

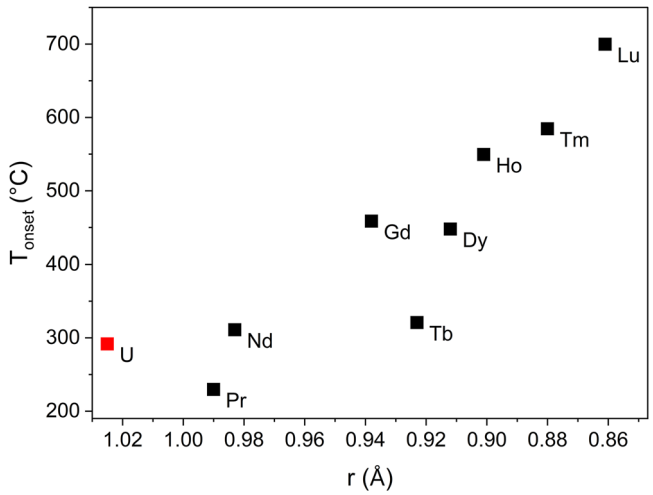

Fig. 10 | Oxidation onset temperatures, Tonset, of U/LnN samples against the cation ionic radius of their associated compound. Oxidation onset temperatures, T_{onset}, of U/*Ln*N (*Ln* = Pr, Nd, Gd, Tb, Dy, Ho, Tm, Lu) samples against the cation ionic radius of their associated compound, based on their reported ionic radii[27] when in a trivalent 6-fold coordination environment. All temperature values have an uncertainty of σ = ± 1 °C given by the used thermocouple type S.

would be more expected and a scenario following b) in Fig. 11 would be more likely.

Discussion

The present investigation has examined the oxidation mechanisms of the binary U^{3+} N and Ln^{3+}N compounds for *Ln* - Pr, Nd, Gd, Tb, Dy, Ho, Tm and Lu, which crystallise in cubic face-centred (rock salt) structures with $Fm\bar{3}m$ space group symmetry, at ambient and high temperature via PXRD, SEM-EDS, isothermal and thermal gravimetric, DSC, U L_3-edge XANES and Pr/Dy L_3-edge HR-XANES experiments. At ambient conditions, UN is found to undergo an oxygen mediated oxidation mechanism involving the successive formation of U_2N_3 and UO_2 phases. Contrastingly, *Ln*N compounds appear to follow consistent hydrolysis-based oxidation mechanisms resulting in the formation of either crystalline or amorphous $Ln^{3+}(OH)_3$ compounds as evidenced by PXRD for *Ln* = Pr and Nd, and by HR-XANES for *Ln* = Dy. The reaction is consequently expected to only proceed in the presence of moisture. At high temperatures, both UN and *Ln*N compounds are found to form oxidised phases of respectively U_3O_8 and Ln_2O_3 type. Additionally, the rate of oxidation at high temperatures appears to correlate with the size of the *Ln*/U cation, such that smaller cations lead to inhibited oxidation rates. Considering the known literature and isostructural chemical behaviour of UN and *Ln*N compounds, solid solutions of these are expected within UN based SNF. However, the results of the investigation suggest that unexpected oxidation of the fuel can result in variable chemical and microstructural behaviour. Pertinently also, although *Ln's* will likely inhibit the rate of oxidation of the UN matrix, pronounced for heavier *Ln*'s, which is overall beneficial to stability against oxidation, the resultant microstructure and chemical assemblage can exhibit significant phase separation and incongruency. Such behaviour contrasts to what readily occurs in UO_2 based SNF when exposed to environments containing oxygen and/or humidity, namely a solid solution of *Ln*'s contained within U oxide matrix. Consequently, the investigation points to the pertinence of the appropriate storage and housing of *Ln*N and UN based compounds within anoxic atmospheres. Moreover, the investigation has provided critical fundamental insight into the chemical behaviour of UN and *Ln*N phases, relevant to next generation UN fuel and subsequent SNF generation.

Table 4 | Summary of TGA-DSC determined onset temperatures T_{onset}, temperatures of the DSC maxima T_{DSC}, experimental and theoretical mass changes and via PXRD analysis determined oxidation products of U/*Ln*N (*Ln* = Pr, Nd, Gd, Tb, Dy, Ho, Tm, Lu) oxidised in air at 900 °C

Compound	T_{onset} (°C) [a]	T_{DSC} (°C)	Δm_{total} (%)	Δm_{theo} (%) (oxidation product)	Oxidation Product
PrN	229.5	283.6 310.6	11.07	11.61(PrO_2)	$PrO_{1.84}$ [b]
NdN	310.9	318.3 445.6 502.2	6.28	6.31 (Nd_2O_3)	Nd_2O_3
GdN	458.6	609.9	5.85	5.83 (Gd_2O_3)	Gd_2O_3
TbN	320.6	323.0 389.2	9.41	9.01 ($TbO_{1.85}$)	$TbO_{1.81}$ [b]
DyN	447.7	564.3	6.13	5.66 (Dy_2O_3)	Dy_2O_3
HoN	549.5	575.5	6.62	5.58 (Ho_2O_3)	Ho_2O_3
TmN	584.5	599.2	6.95	5.46 (Tm_2O_3)	Tm_2O_3
LuN	699.7	822.3	5.34	5.28 (Lu_2O_3)	Lu_2O_3
UN	291.6	383.7 401.5	12.73	13.48 (UO_3)	U_3O_8

All temperature values have an uncertainty of σ = ± 1 °C given by the used thermocouple type S.
[a]Defined as 5% of total mass change of the nitride to oxide reaction.
[b]Oxygen content determined by Rietveld analysis.

Methods

Synthesis of LnN (Ln = Pr, Nd, Gd, Tb, Dy, Ho, Tm, Lu)

The synthesis of lanthanide nitride powders was achieved via nitridation reactions of *Ln* metals. Fine pieces of lanthanide metals (Hunan Rare Earth Metals Materials Co, 99.9%) were placed in tungsten crucibles and heated in flowing nitrogen atmosphere (Nippon Gases, 99.999%, purified with an oxysorb cartridge) utilising a custom water-cooled radio frequency furnace[48]. Nitridation reactions were performed at ambient pressures for 30 minutes in a range of 100 °C below the melting point to the melting point of the individual metals. After the reaction, the completely reacted samples were crushed with tungsten carbide mortars and finely ground in agate mortars. The nitride powders were sieved through a 100 mesh using an argon atmosphere filled glovebox with appropriate oxygen sensors to minimise contamination.

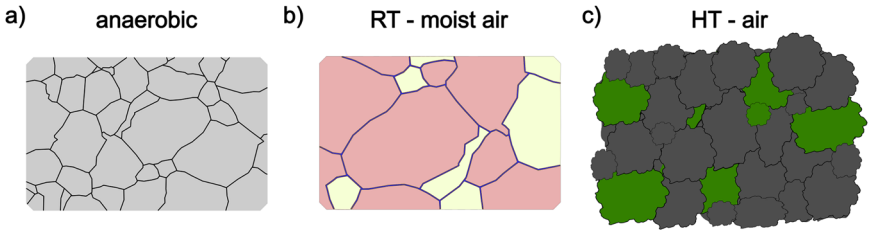

Fig. 11 | Graphical illustration of microstructures of Ln-doped UN in different conditions. Graphical illustration of (**a**) *Ln*-doped UN single phase microstructure expected to occur in irradiated UN fuel under anaerobic conditions, (**b**) *Ln*-doped UN multiphase microstructure expected to occur when irradiated UN fuel is exposed to atmospheric conditions (RT)–wet oxidation; room temperature air and moisture, showing phase separation of UO_2 (red), $Ln(OH)_3$ (yellow) and U_2N_3 (blue lines) and (**c**) *Ln*-doped UN multiphase microstructure of irradiated UN fuel is exposed to high temperature (HT) oxidising conditions, showing formation of expanded particles of U_3O_8 (dark gray) and Ln_2O_3 (green).

Synthesis of UN

Uranium nitride was synthesised by carbothermic reduction of UO_3 followed by direct nitridation. UO_3 powder was obtained using a wet synthesis route, where uranyl nitrate ($UO_2(NO_3)_2$, MERCK, > 99% purity) was precipitated as ammonium diuranate ($(NH_4)_2U_2O_7$, ADU) using ammonia. The ADU was calcined in air at 500 °C for 4 h using a box furnace (Carbolite CWF 13/5, Neuhausen, Germany), resulting in the formation of UO_3 powder. In a next step the UO_3 powder was mixed with C powder (Thermo Scientific, 99.9995% purity) in a molar ratio of 1:2.7. The mixture was calcined at 1500 °C in a high temperature tube furnace (ENTECH ESTF 50-18-SP-VK, Ängelholm, Sweden) using Al_2O_3 crucibles. Heating up and isothermal hold for 4 h were performed with flowing N_2/H_2 gas (Air Liquide, 3.9 Vol% H_2, 99.999% N_2 and 99.9% H_2 purity). Upon completion of the isothermal hold, the mixture was heated to 1650 °C for 30 minutes to remove excess carbon. To cool down the reaction mixture the gas was switched to Ar/H_2 (Air Products, 4 Vol% H_2, 99.9999%) in order to prevent the formation of U_2N_3. The resulting powder had a grey to black colour.

Room temperature oxidation studies

To understand the chemical and structural changes of UN and *Ln*N (*Ln* = Pr, Nd, Gd, Tb, Ho, Tm, Lu) when exposed to air at room temperature, powders of each compound with approximately 20 mg mass as amount were oxidised in laboratory air with standard relative humidity. DyN could not be measured due to sample availability issues. The *Ln*N powders were filled under protective atmosphere into Wheaton™ liquid scintillation counting vials (Perkin Elmer, 20 mL volume, 28 ×61 mm, foiled polypropylene screwcap) and transferred to an analysis balance (Mettler Toledo XP205 DeltraRange). A homogeneous distribution on the circular surface of the vial cap (16 mm diameter) prior to air exposure was achieved by flipping the vial and tapping it on a flat surface. Through unscrewing of the glass body of the vials, the samples were then precisely exposed to air (23 °C, regular air, 40% humidity) whilst on the balance and the weight of the sample carefully monitored in the first 30 s of exposure every 10 seconds, then every 30 seconds until 2 minutes of exposure time was reached. Until 10 minutes of exposure the weight was noted every minute of exposure. The collected weights were used to calculate the weight change of the samples over a period of ten minutes. The data was then analysed via regression analysis to determine the oxidation rate using a linear fit as an approximation, based on observed data trends. Details are provided in Supplementary Information Note 1, Fig. S1 and Table S1. After monitoring the weight for 10 minutes, the samples were left in laboratory air for 1 day (*Ln* = Pr, Nd, Gd) to 3 days (*Ln* = Tb, Dy, Ho, Tm, Lu) to completely oxidise. During this time, the nitride powders changed in colour and a volumetric expansion was observed, which are representatively shown for the oxidation of NdN in Fig. 5.

High temperature oxidation studies—thermogravimetric analysis

To get insight into the high-temperature oxidation behaviour of *Ln*N (*Ln* = Pr, Nd, Gd, Tb, Dy, Ho, Tm, Lu) thermogravimetric measurements were performed using a NETZSCH STA 449 C Jupiter with coupled thermogravimetry and differential scanning calorimetry setup (TGA-DSC) and a Type S thermocouple ($\sigma_T = \pm 1$ °C). Powder samples of 20 mg were placed in Pt/Rh crucibles (NETZSCH) and heated to 900 °C in flowing synthetic air at a 10 °C/min rate. Before cooling at the same rate an isothermal hold for 30 min was performed. The oxidation residues were analysed by PXRD.

Powder X-ray diffraction (PXRD)

PXRD data of pristine and finely ground *Ln*N powders were collected on a Huber G670 imaging plate Guinier camera ($2\Theta_{max} = 100°$) using a curved germanium (111) monochromator and Cu-$K_{\alpha 1}$ (*Ln* = Pr, Nd, Tb, Dy, Ho, Tm, Lu) or Co-$K_{\alpha 1}$ radiation (*Ln* = Gd) at 293(1) K. The powder samples were placed between Kapton foils to avoid degradation in air. PXRD data of the pristine UN, oxidised UN and oxidised *Ln*N (*Ln* = Pr, Nd, Gd, Tb, Dy, Ho, Tm, Lu) samples were collected on a Bruker D4 Endeavor diffractometer equipped with a *1D* Lynx-eye detector in Bragg–Brentano configuration using Cu$K_{\alpha 1,2}$ radiation ($\lambda = 1.54184$ Å) at room temperature. Fine ground powder samples were placed on a thin Vaseline layer on Si-zero background holders, closed by an airtight Kapton dome. Measurements were performed in the range of $20° \leq 2\theta \leq 85°$ with a step size of $(2\theta) = 0.02°$ and a counting time of 3 s per step. Data analysis was performed via the Rietveld and Le Bail methods as implemented in the program GSAS-II[49].

Pr and Dy L3-edge high-energy resolution X-ray absorption near-edge structure spectroscopy

HR-XANES experiments at the *Ln* L_3-edge of pristine, partially oxidised and fully oxidised PrN and DyN pellets of approximately 50 mg were recorded at the SUL-X beamline at the KIT Light Source, Karlsruhe Institute of Technology (KIT), Karlsruhe, Germany. The partially and fully oxidised nitride materials were produced by exposure of sample material to air for 1 hour and 24 h respectively. Pellets of the pristine and oxidised nitrides were pressed under inert atmosphere and mounted onto modified cryostat cells originally designed for use at the ACT beamline[50]. Samples were then transported to the beamline under inert atmosphere using airtight transport bottles. Radiation from a 27-pole wiggler is monochromatized in the beamline with a fixed-exit Si(111) double crystal monochromator (DCM) and focused to about 1.2 mm vertical and 1.2 mm horizontal at sample position. Sample fluorescence was collected with an X-ray emission spectrometer in focusing horizontal Rowland circle geometry using a single striped, spherically bent analyser crystal with a bending radius of 0.5 m. For Pr L_3 a Si(331) crystal (produced at the ESRF) and for Dy L_3, the (444) reflection of a Ge(111) crystal (XRS TECH) was used. For detection, a fast silicone drift detector (Amptek, XR-100fastSDD) with a 70 μm Kapton window at the maximum of the Pr L_3M_5 (at 5033.3 eV, with a Bragg angle of 81.83°) and Dy $L_3N_{4,5}$ (at 7635.9 eV, with a Bragg angle of 70.99°) emission lines was used respectively[51]. The sample, crystal and detector were positioned with an 8° tilt with respect to the Rowland circle and a 180° angle between the incoming beam and the sample-crystal plane[52]. The spectrometer was

aligned with the known emission energies of metal references (for Pr: Pr L_3M_5 at 5033.3 eV and Cr KL_3 at 5414.7 eV, for Dy using Nd L_2M_4 at 5721.6 eV and Fe KL_3 at 6403.9 eV)[51]. After alignment, elastic lines were used to determine a spectrometer resolution of 1 eV at an energy of 5033 eV for Pr measurements and 1.3 eV at an energy of 7650 eV for Dy measurements. Measurements were performed under high vacuum (10^{-5} mbar range) and liquid nitrogen cooling. Radiation stability was tested by collecting a series of HR-XANES spectra (eight 30 second scans, followed by ten four-minute scans) and monitoring the spectral profile for changes. No changes were observed in this timeframe. Subsequent measurements were then performed on fresh sample spots and limited to the proven stable timeframes. Calibration of the excitation energy axis took place using repeated XANES transmission measurements of metal foils (V K-edge at 5465.1 eV (PyMCA) for Pr, Co K-edge at 7708.9 eV (PyMCA) for Dy)[51]. The first intense maxima of the first derivative spectra, corresponding to the first inflection point of the spectra, were assigned to the tabulated values of the absorption edges of V and Co. Emission energies were calibrated using the emission lines of Dy_2O_3 and $PrCl_3$ references[51]. HR-XANES data were processed by merging and normalizing using ATHENA from the DEMETER program package and exporting the normalized, not flattened spectrum[53]. Further data analysis was performed in OriginLab's OriginPro 2025.

U L3-edge X-ray absorption near-edge structure spectroscopy

Two partially oxidised UN samples received from synthesis attempts with accidental oxygen ingress during the runs were used to perform U L_3-edge XANES experiments at the ROBL[54] beamline at the European synchrotron radiation facility (ESRF) in Grenoble, France. The incident energy was scanned using a water-cooled Si(111) DCM around the corresponding edge. Two Rh mirrors, positioned before and after the monochromator, were used to collimate the beam, reject higher harmonics, and focus it on the sample. Prior to measurement, the UN samples were ground into a powder, mixed with boron nitride at a weight ratio of 1:10, and then pressed into pellets. All measurements were performed at 25 °C.

Electron microscopy

The morphology and composition of the oxidised UN and *Ln*N powders were determined using an Apreo 2 C LoVac scanning electron microscope (ThermoFisher Scientific, Netherlands) equipped with an Octane elect PLUS Silicon Drift Detector (EDAX, Weiterstadt, Germany). The powders were distributed on carbon-based sample holders after oxidation without any further treatment. Backscattered electron (BSE) images as well as EDS spot measurements and elemental mappings were collected at 20 kV and 1.2 or 3.2 nA at a working distance of 10 mm.

Data availability

The data that support the findings of this study is available in an open access Zenodo repository, DOI: 10.5281/zenodo.20120347.

Received: 27 February 2026; Accepted: 6 June 2026;
Published online: 16 June 2026

References

1. Kelly, J. E. Generation IV international forum: a decade of progress through international cooperation. *Prog. Nucl. Energy* **77**, 240–246 (2014).
2. Dehlin, F., Wallenius, J. & Bortot, S. An analytic approach to the design of passively safe lead-cooled reactors. *Ann. Nucl. Energy* **169**, 108971 (2022).
3. Elkhawas, N. A., Reda, S. M., Amin, E. A. & Anwar, D. Deployment study of accident tolerant fuels in small modular advanced high temperature reactor. *Phys. Scr.* **100**, 095307 (2025).
4. Degueldre, C., Goddard, D., Berhane, G., Simpson, A. & Boxall, C. Simulation of uranium mononitride spent fuel: a thermodynamic approach. *J. Nuclear Mater.*, 154900 (2024).
5. Degueldre, C., Goddard, D. T., Berhane, G., Simpson, A. & Boxall, C. Simulation of uranium mononitride spent fuel: A crystallographic approach. *J. Nucl. Mater.* **562**, 153612 (2022).
6. Dehadraya, J. V. et al. The oxidation of uranium-cerium mononitride microspheres. *J. Alloy. Compd.* **257**, 313–321 (1997).
7. Vinograd, V. L., Bukaemskiy, A. A., Deissmann, G. & Modolo, G. Thermodynamic model of the oxidation of *Ln*-doped UO_2. *Sci. Rep.* **13**, 17944 (2023).
8. Murphy, G. L. et al. Probing the long- and short-range structural chemistry in the C-type bixbyite oxides Th0.40Nd0.48Ce0.12O1.76, Th0.47Nd0.43Ce0.10O1.785, and Th0.45Nd0.37Ce0.18O1.815 via synchrotron X-ray diffraction and absorption spectroscopy. *ACS Omega* **9**, 27397–27406 (2024).
9. Shirokiy, D. et al. Speciation and radiation stability of Cr and Ln "Grey-Phases" within Cr-doped (Ln,U)O2 spent fuel model materials. *npj Mater. Degrad.* https://doi.org/10.1038/s41529-026-00752-5 (2026).
10. Holmes-Hewett, W. F., Miller, J. D., Ahmad, H. G., Granville, S. & Ruck, B. J. Rare-earth nitrides: fundamental advances and applications in cryogenic electronics. *J. Phys. D: Appl. Phys.* **58**, 343001 (2025).
11. Xiao, K., Shi, X., Zhang, X., Ping, Q. & Du, L. The emergence of novel magnetic properties in ternary iron nitrides toward spintronics: first-principles calculations. *Phys. Chem. Chem. Phys. PCCP* **27**, 6677–6686 (2025).
12. Kwon, H. R., Yang, J. W. & Jang, H. W. Metal nitride catalysts for photoelectrochemical and electrochemical catalysis. *Exploration* **5**, 20240013 (2025).
13. Porter, W. N., Turaczy, K. K., Yu, M., Mou, H. & Chen, J. G. Transition metal nitride catalysts for selective conversion of oxygen-containing molecules. *Chem. Sci.* **15**, 6622–6642 (2024).
14. Fahrenholtz, W. G. & Hilmas, G. E. Ultra-high temperature ceramics: materials for extreme environments. *Scr. Mater.* **129**, 94–99 (2017).
15. Wan, Y. et al. A nitride-reinforced NbMoTaWHfN refractory high-entropy alloy with potential ultra-high-temperature engineering applications. *Engineering* **30**, 110–120 (2023).
16. Kneisel, K. et al. Synthesis, structural, and Raman investigation of lanthanide nitride powders (*Ln* = La, Ce, Nd, Sm, Gd, Tb, Dy, Er, Lu). *ACS omega* **9**, 47842–47847 (2024).
17. Dell, R. M., Wheeler, V. J. & McIver, E. J. Oxidation of uranium mononitride and uranium monocarbide. *Trans. Faraday Soc.* **62**, 3591 (1966).
18. Watkins, J. K., Gonzales, A., Wagner, A. R., Sooby, E. S. & Jaques, B. J. Challenges and opportunities to alloyed and composite fuel architectures to mitigate high uranium density fuel oxidation: Uranium mononitride. *J. Nucl. Mater.* **553**, 153048 (2021).
19. Lawrence Bright, E. et al. Oxidation and passivation of the uranium nitride (001) surface. *Corrosion Sci.* 110705 (2022).
20. Sole, M. J. & Van Der Walt, C. M. Oxidation and deformation studies of uranium nitride by electron microscopy. *Acta Metall.* **16**, 501–510 (1968).
21. Paljević, M. & Despotović, Z. Oxidation of uranium mononitride. *J. Nucl. Mater.* **57**, 253–257 (1975).
22. Goncharov, V. G. et al. Energetics of oxidation and formation of uranium mononitride. *J. Nucl. Mater.* **569**, 153904 (2022).
23. Vinograd, V. L., Bukaemskiy, A. A., Modolo, G., Deissmann, G. & Bosbach, D. Thermodynamic and structural modelling of non-stoichiometric Ln-doped UO2 solid solutions, Ln={La, Pr, Nd, Gd}. *Front. Chem.* **9**, 705024 (2021).
24. Liu, J. et al. Thermal expansion and steam oxidation of uranium mononitride analysed via in situ neutron diffraction. *J. Nucl. Mater.* **575**, 154215 (2023).
25. Rundle, R. E., Baenziger, N. C., Wilson, A. S. & McDonald, R. A. The structures of the carbides, nitrides and oxides of uranium. *J. Am. Chem. Soc.* **70**, 99–105 (1948).

26. Kai, H., Katsura, M. & Sano, T. Nitrogen pressure region for monophase UC -UN solid solution and relation of its lattice parameter and composition. (1969).
27. Shannon, R. D. Revised effective ionic radii and systematic studies of interatomic distances in halides and chalcogenides. *Acta Crystallogr. Sect. A* **32**, 751–767 (1976).
28. Baur, W. H. Effective ionic radii in nitrides. *Crystallogr. Rev.* **1**, 59–83 (1987).
29. Olcese, G. L. Interconfiguration fluctuation of cerium in CeN as a function of temperature and pressure. *J. Phys. F: Met. Phys.* **9**, 569–578 (1979).
30. Kappler, J. P. et al. Anomalous behaviour of X-ray absorption observed on the highly correlated cerium nitride (CeN) compound. *J. de. Phys. I* **1**, 1381–1387 (1991).
31. Natali, F. et al. Rare-earth mononitrides. *Prog. Mater. Sci.* **58**, 1316–1360 (2013).
32. Wan, Y. et al. Structure and oxidation properties of CeN thin films prepared by DC reactive magnetron sputtering. *Surf. Coat. Technol.* **381**, 125168 (2020).
33. Ikawa, K. & Taketani, K. Room temperature oxidation of UN powder. *J. Nucl. Sci. Technol.* **7**, 433–438 (1970).
34. Beňadik, A. Atmospheric corrosion of uranium monocarbide, mononitride, and carbonitrides. *Collect. Czechoslovak Chem. Commun.* **35**, 988–993 (1970).
35. Murphy, G. L. et al. Deconvoluting Cr states in Cr-doped UO_2 nuclear fuels via bulk and single crystal spectroscopic studies. *Nat. Commun.* **14**, 2455 (2023).
36. Ramanantoanina, H. et al. High-energy resolution X-ray spectroscopy reveals bonding characteristics of La^{3+} homologues of actinium radiopharmaceuticals. *Commun. Chem.* https://doi.org/10.1038/s42004-026-01929-4 (2026).
37. Gouder, T., Seibert, A., Rebizant, J., Huber, F. & Havela, L. Comparative photoemission study of actinide (Am, Pu, Np and U) metals, nitrides, and hydrides. *MRS Proceedings* **986** https://doi.org/10.1557/proc-986-0986-oo01-02 (2006).
38. Irber, W. The lanthanide tetrad effect and its correlation with K/Rb, Eu/Eu*, Sr/Eu, Y/Ho, and Zr/Hf of evolving peraluminous granite suites. *Geochim. Cosmochim. Acta* **63**, 489–508 (1999).
39. Fleming, P., Farrell, R. A., Holmes, J. D. & Morris, M. A. The rapid formation of La(OH) 3 from La2O3 powders on exposureto water vapor. *J. Am. Ceram. Soc.* **93**, 1187–1194 (2010).
40. Rao, G. A. R., Mukerjee, S. K., Vaidya, V. N., Venugopal, V. & Sood, D. D. Oxidation and hydrolysis kinetic studies on UN. *J. Nucl. Mater.* **185**, 231–241 (1991).
41. Kulyukhin, S. A., Nevolin, Y. M., Gordeev, A. V. & Bessonov, A. A. Gas-phase volume oxidation of uranium mononitride. *Radiochemistry* **61**, 146–155 (2019).
42. Arai, Y., Maeda, A., Shiozawa, K. -i & Ohmichi, T. Chemical forms of solid fission products in the irradiated uranium—plutonium mixed nitride fuel. *J. Nucl. Mater.* **210**, 161–166 (1994).
43. Uno, M., Kurosaki, K., Yamanaka, S. & Minato, K. Thermal properties of simulated high burn up nitride fuels and nitride ADS targets. *MRS Proc.* **1043**. https://doi.org/10.1557/proc-1043-t13-03.
44. Smailos, E. Reactions of fission products in carbide and nitride fuel based on simulated experiments. Report No. KFK 1953, (Kernforschungszentrum Karlsruhe, 1974).
45. Holleck, H., Smailos, E. & Thümmler, F. Zur Mischkristallbildung von UN mit den Nitriden der Seltenen Erden CeN und NdN. *J. Nucl. Mater.* **28**, 105–109 (1968).
46. Holleck, H., Smailos, E. & Thümmler, F. Zur Mischphasenbildung der Mononitride in den Systemen U- (Y, La, Pr)-N. *J. Nucl. Mater.* **32**, 281–289 (1969).
47. Giacchetti, G., Sari, C. & Walker, C. T. Actinides and fission products distribution in fast breeder nitride fuel. *Nucl. Technol.* **28**, 216–225 (1976).
48. Schnick, W., Huppertz, H. & Lauterbach, R. High temperature syntheses of novel nitrido- and oxonitrido-silicates and sialons using rf furnaces. *J. Mater. Chem.* **9**, 289–296 (1999).
49. Toby, B. H. & Dreele, R. B. v. GSAS-II: the genesis of a modern open-source all purpose crystallography software package. *J. Appl. Crystallogr.* **46**, 544–549 (2013).
50. Schacherl, B. et al. Implementation of cryogenic tender X-ray HR-XANES spectroscopy at the ACT station of the CAT-ACT beamline at the KIT Light Source. *J. Synchrotron Radiat.* **29**, 80–88 (2022).
51. Solé, V. A., Papillon, E., Cotte, M., Walter, P. & Susini, J. A multiplatform code for the analysis of energy-dispersive X-ray fluorescence spectra. *Spectrochim. Acta Part B At. Spectrosc.* **62**, 63–68 (2007).
52. Schacherl, B. et al. Resonant inelastic X-ray scattering tools to count 5 f electrons of actinides and probe bond covalency. *Nat. Commun.* **16**, 1221 (2025).
53. Ravel, B. & Newville, M. ATHENA, ARTEMIS, HEPHAESTUS: data analysis for X-ray absorption spectroscopy using Ifeffit. *J. Synchrotron Radiat.* **12**, 537–541 (2005).
54. Scheinost, A. C. et al. ROBL-II at ESRF: a synchrotron toolbox for actinide research. *J. Synchrotron Radiat.* **28**, 333–349 (2021).
55. Brown, R. C. & Clark, N. J. Composition limits and vaporization behaviour of rare earth nitrides. *J. Inorg. Nucl. Chem.* **36**, 2507–2514 (1974).
56. Ettmayer, P., Waldhart, J., Vendl, A. & Banik, G. Über die Mischkristallbildung von ThN mit LaN, CeN, PrN, NdN, SmN, GdN, DyN und ErN. *Monatshefte f.ür. Chem.* **111**, 945–948 (1980).
57. Klesnar, H. & Rogl, P. F. Phase relations in the ternary systems rare-earth metal (*RE*)-boron-nitrogen, where *RE*=Tb. *Dy Ho Er Tm. Lu Sc. Y. high. Temp.High. Press.* **22**, 453–457 (1990).
58. Mullica, D. F., Milligan, W. O. & Beall, G. W. Crystal structures of $Pr(OH)_3$, $Eu(OH)_3$ and $Tm(OH)_3$. *J. Inorg. Nucl. Chem.* **41**, 525–532 (1979).
59. Beall, G. W., Milligan, W. O., Dillin, D. R., Williams, R. J. & McCoy, J. J. Refinement of neodymium trihydroxide. *Acta Crystallogr. Sect. B Struct. Crystallogr. Cryst. Chem.* **32**, 2227–2229 (1976).
60. Desgranges, L., Baldinozzi, G., Rousseau, G., Nièpce, J.-C. & Calvarin, G. Neutron diffraction study of the in situ oxidation of UO_2. *Inorg. Chem.* **48**, 7585–7592 (2009).
61. Sasa, Y. & Atoda, T. Nonstoichiometric hexagonal close-packed uranium sesquinitride. *J. Am. Ceram. Soc.* **53**, 102–105 (1970).

Acknowledgements

Financial support for this research was provided by European Commission through the "Fuel Recycle and Experimentally Demonstrated Manufacturing of Advanced Nuclear Solutions for Safety" (FREDMANS) project, grant agreement number 101060800. Views and opinions expressed are those of the author(s) only and do not necessarily reflect those of the European Union, European Commission or European Atomic Energy Community (granting authority). Neither the European Union nor the granting authority can be held responsible for them. The authors thank Dr Andreas Wilden for his continuous support by providing and maintaining the function of a glovebox workspace necessary to perform the sample preparations of parts of this work. Tonya Vitova and Emily Reynolds gratefully acknowledge financial support from the Deutsche Forschungsgemeinschaft (DFG, German Research Foundation) through the Collaborative Research Centre ″4f for Future" project A1 (CRC 1573, project number 471424360). We thank the Institute for Beam Physics and Technology (IBPT) for the operation of the storage ring, the Karlsruhe Research Accelerator (KARA) and the KIT Light Source for provision of beamtime. The ESRF is also thanked for providing beamtime at ROBL BM20 a part of proposal number A20-1-903.

Author contributions

The research methodology, experimental planning and formal analysis was developed and conducted by P.U. and G.L.M. Funding acquisition and

project management was performed by P.U., C.S. and G.M. The materials were synthesized by P.U., P.H. and P.K. PXRD measurements and analysis were performed by P.U., P.K., P.H. and G.L.M. SEM measurements were performed by P.U., C.E and M.K. Thermogravimetric measurements were performed by P.U. and C.S. The research methodology and planning of the HR-XANES experiments was conducted by R.S., T.V., and L.W. HR-XANES experiments were conducted by P.U., E.R., S.M.S., M.B., J.G., and R.S. For HR-XANES, data analysis was done by E.R. and T.V., and data visualisation was done by E.R. and P.U. XANES experiments were conducted by G. L.M., D.P. and N.H. Manuscript writing, review and editing was performed by P.U. and G.L.M with input from all authors.

Funding

Open Access funding enabled and organized by Projekt DEAL

Competing interests

The authors declare no competing interests.

Additional information

Supplementary information The online version contains supplementary material available at https://doi.org/10.1038/s41529-026-00827-3.

Correspondence and requests for materials should be addressed to Pascal Uhlemann or Gabriel L. Murphy.